UC San Diego
International Symposium on Stratified Flows

Title

Radiation of internal waves by symmetrically unstable fronts

Permalink

Journal

Authors

Grisouard, Nicolas
Fox, Morgan B.
Nijjer, Japinder

Publication Date

Radiation of Internal Waves by Symmetrically Unstable Fronts

Nicolas Grisouard[1], Morgan B. Fox[2,1] and Japinder Nijjer[3]

[1] Dept. of Physics, University of Toronto, ON, Canada (nicolas.grisouard@utoronto.ca)
[2] Engineering Physics program, Queen's University, Kingston, ON, Canada.
[3] Dept. of Applied Mathematics and Theoretical Physics, University of Cambridge, UK.

Abstract

Most of the ocean's kinetic energy exists in the form of mesoscale eddies in geostrophic and hydrostatic balance. Because of their relatively large horizontal size, they tend to be dynamically robust, and it is unclear how they dissipate their energy. Submesoscale oceanic density fronts are believed to be hotspots for such dissipation processes, but their dynamics are poorly known. We present preliminary results about a mechanism through which a front loses energy by releasing it in the form of internal inertia-gravity waves. A mid-latitude, submesoscale ocean density front is set up to be symmetrically unstable over a confined region of space. If the growth rate is large enough, the growth phase is accompanied by significant near-inertial wave radiation, which we illustrate numerically.

1 Introduction

Oceanic density fronts are places of intense kinetic energy dissipation (D'Asaro et al., 2011), which could have significant implications in closing the energy budget of the ocean (see e.g. Ferrari and Wunsch, 2009; McWilliams, 2016). They are also small (O(10 km) at mid-latitudes) and ephemeral (O(day)), and are therefore hard to observe. An oceanic density front is typically characterized by a vertical density gradient $\partial_z\bar\rho$, where z is the vertical coordinate and $\bar\rho$ the unperturbed density field, or equivalently by a buoyancy frequency $N = \sqrt{-(g/\rho_0)\partial_z\bar\rho}$, where $g = 9.81$ m^2 s^{-1} is the gravitational acceleration and $\rho_0 = 1025$ kg m^{-3} a reference density. But a front is also characterized by a lateral density gradient $\partial_x\bar\rho$, where x is the across-front direction, such that one can define $M^2 = -(g/\rho_0)\partial_x\bar\rho$. In the across-front direction, geostrophic and hydrostatic balances usually hold approximately. Indeed, differential Coriolis forces induced by a vertically sheared along-front velocity, $\bar v$, approximately balance the baroclinic torque caused by the lateral density gradient. In short, they are in thermal wind balance: $\mathrm{d}\bar v/\mathrm{d}z = M^2/f$, where f is the Coriolis frequency (assumed constant in this communication).

Because of their relatively short width, however, their Rossby and Richardson numbers,

$$\overline{\mathrm{Ro}} = \partial_x\bar v/f \quad \text{(Rossby number)} \quad \text{and} \quad \overline{\mathrm{Ri}} = N^2/|\partial_z\bar v|^2 \quad \text{(Richardson number)}, \quad (1)$$

are of order unity. Consequently, they are likely to undergo various instabilities (e.g., Haine and Marshall, 1998; Boccaletti et al., 2007; Wang et al., 2014; Arobone and Sarkar, 2015), and in particular, symmetric instability (SI). SI occurs in the mixed layer of the ocean when isopycnals steepen so much that the product of the Ertel potential vorticity (EPV), $\overline Q$, with f is negative (e.g., Haine and Marshall, 1998; Taylor and Ferrari, 2009; Thomas et al., 2013). We use the convention:

$$f\overline Q = f\boldsymbol\nabla\bar b \cdot (\boldsymbol\nabla \times \bar v\hat{\mathbf y}) = \overline{\mathrm{Ro}}f^2N^2 - M^4 < 0, \quad (2)$$

where $\bar b = -g(\bar\rho - \rho_0)/\rho_0$ and $\hat{\mathbf y}$ is the unity vector that orients the along-front direction.

More recently, the role of internal waves, and in particular near-inertial waves (NIWs, i.e., internal waves whose frequency is near f), has been investigated for potentially driving energy dissipation in fronts, although narratives are still incomplete. Near-inertial waves tend to accumulate in fronts, which has been observed *in situ* (e.g., Kunze and Sanford, 1984; Rainville and Pinkel, 2004; Joyce et al., 2013) and interpreted theoretically (Whitt and Thomas, 2013). Theoretical studies also indicate that a pre-existing NIW field can extract energy from fronts, for example through parametric subharmonic instability (Thomas and Taylor, 2014) or via dissipative processes occurring when NIWs reflect against the ocean surface (Grisouard and Thomas, 2016). Other theoretical studies suggest that geostrophic flows can radiate internal waves, extracting energy during frontogenesis and/or rapid loss of balance (Thomas, 2012; Shakespeare and Taylor, 2014). Observations of internal wave radiation from fronts are challenging and therefore scarce, to the notable exception of Alford et al. (2013).

We here document a mechanism of radiation of internal waves from fronts, which is distinct from the ones cited above. A front is initially set up in a non-linear, non-hydrostatic Boussinesq numerical model such that $f\overline{Q} < 0$ in some finite region of space. As a result, SI develops, with its typical along-isopycnal motions. However, most of the idealized studies on SI previously cited have setups that are homogeneous in at least one spatial direction. SI in our case expands outward from a localized region in space. In the cases investigated in this communication, this localized, non-stationary phenomenon is shown to be a source of NIW radiation. This communication is organized as follows. In § 2, we present some basic theoretical facts about SI and NIWs, which help provide qualitative explanations of the process at stake. In § 3, we introduce the setup of our experiments. In § 4, we present a numerical illustration of the process at stake. These preliminary results hint at additional questions and perspectives, which we discuss in § 5.

2 Theoretical considerations

The original linear stability analysis of Stone (1966) helps understanding the connection between SI and NIWs in fronts. We start from the linear, hydrostatic, inviscid Boussinesq equations, expanded around a geostrophic flow, $\bar{v}$, and the corresponding buoyancy gradient at rest, $\boldsymbol{\nabla}\bar{b} = (M^2, N^2)$. We only consider motions that have variations in x and z, not y, and geostrophic flows for which $\overline{\mathrm{Ro}}$, M^2, and N^2 are constant in space and time. Consequently, $\bar{v}$ only depends on z. The equations are (e.g., Whitt and Thomas, 2013):

$$\partial_t u - fv + \partial_x p = 0, \quad \partial_t v + f\left(1 + \overline{\mathrm{Ro}}\right)u + M^2 w/f = 0, \quad -b + \partial_z p = 0, \quad (2a)$$

$$\partial_t b + M^2 u + N^2 w = 0 \quad \text{and} \quad \partial_x u + \partial_z w = 0. \quad (2b)$$

$\boldsymbol{v} \equiv (u, v, w)$ is the velocity vector of the perturbations about $\bar{v}$ along with its Cartesian projections, and p is the pressure divided by ρ_0. Eliminating the pressure by virtue of the hydrostatic balance and substituting a plane-wave Ansatz, namely $\{\boldsymbol{v}, b\} = \{\boldsymbol{v}_0, b_0\} \exp \mathrm{i}[kx + mz - (\omega + \mathrm{i}\sigma)t]$, where k, m, ω and σ are all real numbers, into the equations above yields a linear system of equations. Canceling the determinant yields:

$$\omega + \mathrm{i}\sigma = \pm\sqrt{f\overline{Q}/N^2 + N^2\left(\alpha + \beta\right)^2}, \quad (3)$$

where $\beta = M^2/N^2$ and $\alpha = -k/m$. Notice that the equation above can only be either purely real, or purely imaginary, which yields either the dispersion relationship for internal

waves in a geostrophic flow or the growth rate of SI, respectively. We find here that a necessary condition for SI is indeed $f\overline{Q} < 0$, and that if $\overline{\text{Ro}} = 0$ and $M^2 = \beta = 0$, then $f\overline{Q} = f^2 N^2$, $\sigma = 0$ and the classical hydrostatic dispersion relationship for internal waves is recovered. In the situation where $f\overline{Q} < 0$, and where α is such that $\omega = 0$ and $\sigma \neq 0$, then an instability grows. The fastest growing modes are such that $\alpha = -\beta$, that is, have motions aligned with isopycnals, and grow at a rate of

$$\sigma_0 = \sqrt{-f\overline{Q}/N^2}. \tag{4}$$

Although this growth rate only depends on the orientation of the mode, including viscous and hyperviscous terms in the equations implies that the effective rate of growth, seen in a given simulation, is the one that maximizes:

$$\tilde{\sigma} = \sigma - \nu(k^2 + m^2) - \nu_{2h}k^4 - \nu_{2z}m^4, \tag{5}$$

with ν the Laplacian viscosity, ν_{2h} and ν_{2z} the horizontal and vertical hyperviscosities, respectively. In effect, and as a rule of thumb, the fastest growing mode in a given configuration will be the largest one that fits in the $f\overline{Q} < 0$ region.

Outside of the $f\overline{Q} < 0$ region, however, $\sigma = 0$, and the only perturbations allowed are internal waves. As SI grows and propagates towards the boundary between the two regions, it, therefore, has the potential to force internal waves. Once the SI-induced flow has reached this boundary and saturates, then the instability is quasi-stationary, and internal wave generation stops. We now illustrate this scenario with two-dimensional, non-linear, non-hydrostatic numerical simulation, whose setup we describe next.
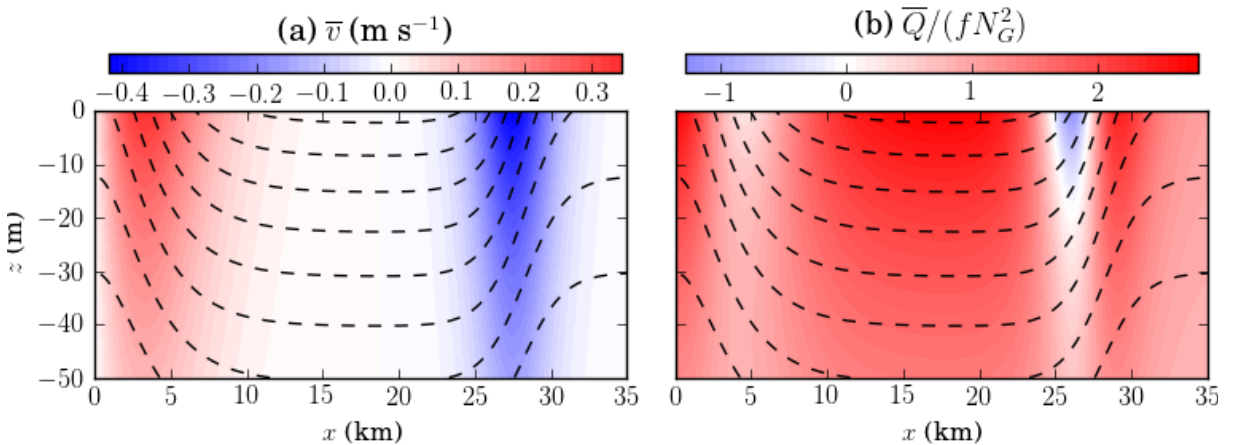
3   Setup

3.1   Physical Setup

Figure 1: Our basic geostrophic flow. In both panels, dashed lines are isopycnal (or iso-$\bar{b}$) contours. (a) geostrophic velocity $\bar{v}$ and (b) Normalized EPV, highlighting the anticyclonic region where $f\overline{Q} < 0$. The EPV contours closely follow those of σ_0, with $\max(\sigma_0/f) \approx 0.72$. Note that the absolute value of $\bar{v}$ is not imposed by our equations. For the purpose of this illustration, we choose the level for which $\bar{v} = 0$ to be at $z = -5$ km, without it having any consequence on the results.

The main physical features of our setup are summarized in fig. 1. Our domain is two-dimensional, periodic in x, has x- and $y-$axes that align with the across- and along-geostrophic flow directions, respectively, while the z-axis points upward, with the ocean

surface located at $z = 0$. Its dimensions are $L_x \times L_z = 35 \text{ km} \times 50 \text{ m}$. Rigid lids close the domain on top and bottom. We solve equations on the f-plane, with $f = 1.03 \times 10^{-4} \text{ s}^{-1}$, corresponding to a latitude of 45°N. We define a buoyancy field in geostrophic balance and featuring a region where $f\overline{Q} < 0$, namely:

$$\overline{b} = \int_0^z N_1^2(\xi)\mathrm{d}\xi + \widehat{B}\,\Gamma(x)\exp(z/\delta), \tag{6}$$

from which we define all other geostrophic quantities. In the expression above, $N_1(z)$ is the buoyancy frequency away from any front. We use the same stratification profile as Gill (1984) and Hazewinkel and Winters (2011), namely:

$$N_1(z) = \frac{N_G}{1 - z/z_G}, \quad \text{with } N_G^2 = 4.9 \times 10^{-5} \text{ s}^{-2} \text{ and } z_G = 400 \text{ m}. \tag{7}$$

$\Gamma(x)$ is the non-dimensional horizontal shape of the frontal system and $\widehat{B}$ is the dimensional measure of the buoyancy difference induced by the presence of a density front below the surface of the domain. The e-folding depth scale over which the geostrophic flow penetrates is $\delta = 50$ m. Our unstable front is located around $x_0 = 27.5$ km. However, because the numerical code requires a horizontally periodic flow and density field, we design a secondary front toward the beginning of the domain, which is stable, and which ensures that e.g. $\overline{b}$, $\overline{v}$, $\overline{\text{Ro}}$ and M^2 are equal at $x = 0$ and $x = L_x$. That is, we define $\Gamma = \Gamma_0 + \Gamma_1$, with:

$$\Gamma_0 = \frac{1}{2}\left[1 - \tanh\left(\frac{x - x_0}{\chi_0}\right)\right] \quad \text{and} \quad \Gamma_1 = -\text{sech}^2\left(\frac{x}{\chi_1}\right), \tag{8}$$

where Γ_0 is the shape of the unstable front and Γ_1 is that of the front that ensures periodicity of the basic geostrophic flow. Their respective widths are χ_0 and χ_1. The latter is determined *ad hoc* as the smallest value that ensures $\min(f\overline{Q}) > 0$ outside of the unstable region and is computed after Γ_0 is. Equations (6), (7) and (8) contain two more free parameters that are yet to be determined, namely the horizontal buoyancy difference $\widehat{B}$ and the width of the unstable front, χ_0. Together with δ, they determine the strength of the front. We set $\widehat{B} = 4.53 \times 10^{-3} \text{ m s}^{-2}$ and $\chi_0 = 2615$ m, implying that our unstable front is characterized by $\max(\overline{\text{Fr}}) = \max(\overline{\text{Ri}}^{-1/2}) = 1.2$ (Froude number) and $\max(\overline{\text{Ro}}) = 1.2$, typical of submesoscale flows. Under these conditions, $\chi_1 = 5$ km. As a result, a region characterized by $f\overline{Q} < 0$ is set up, associated with $\max(\sigma_0) \approx 0.72f$ (eqn. 4, fig. 1).

3.2 Numerical Setup

Our numerical model is a pseudospectral, nonlinear, non-hydrostatic code initially described by Winters et al. (2004). The set of equations, solved by the code, differs from eqns. (3) in that it is fully non-linear, non-hydrostatic, and include dissipation terms:

$$\mathrm{D}_t\boldsymbol{v} + f\hat{\mathbf{z}} \times \boldsymbol{v} + (M^2 w/f + f\overline{\text{Ro}}\,u)\hat{\mathbf{y}} - b\hat{\mathbf{z}} + \boldsymbol{\nabla}p = \mathcal{D}\boldsymbol{v}, \tag{8a}$$

$$\mathrm{D}_t b + M^2 u + N^2 w = \mathcal{D}b \quad \text{and} \quad \partial_x u + \partial_z w = 0, \tag{8b}$$

where $\mathrm{D}_t \equiv \partial_t + (\boldsymbol{v} \cdot \boldsymbol{\nabla})$, $\boldsymbol{\nabla} \equiv (\partial_x, 0, \partial_z)$, and $\mathcal{D} \equiv \nu_h\partial_x^2 + \nu_z\partial_z^2 - \nu_{2h}\partial_x^4 - \nu_{2z}\partial_z^4$. We use $\nu_h = \nu_z = 10^{-5} \text{ m}^2\text{ s}^{-1}$, $\nu_{2h} = 2 \times 10^3 \text{ m}^4\text{ s}^{-1}$ and $\nu_{2z} = 10^{-7} \text{ m}^4\text{ s}^{-1}$. Note that the damping rate of velocity and buoyancy fluctuations is the same. Free-slip and no-buoyancy-fluctuation boundary conditions are implemented at the top and bottom, where we also taper off the frontal terms (Winters and de la Fuente, 2012).

We employ a grid of $n_x \times n_z = 1024 \times 513$ points, corresponding to spatial resolutions of $\Delta x \times \Delta z \approx 34.28$ m $\times$ 97.7 cm, with a time step $\Delta t = 125$ s. We initialize the simulation with random noise and integrate it for 1.8×10^6 s (about 20 days, or 30 inertial periods).

4 Numerical Results

Figure 2 summarizes the process at stake, which we propose to separate into four stages. In the initial stage (panel a), SI grows, with its characteristic isopycnal motion. This stage's duration has an inverse time scale of $\max(\sigma_0) \approx 0.72f$. Therefore, it lasts for a few inertial periods, an inertial period being $T_f = 2\pi/f \approx 61000$ s. During this phase, the instability propagates from the nucleus where the growth rate is maximum and fills up the region where $f\overline{Q} < 0$.
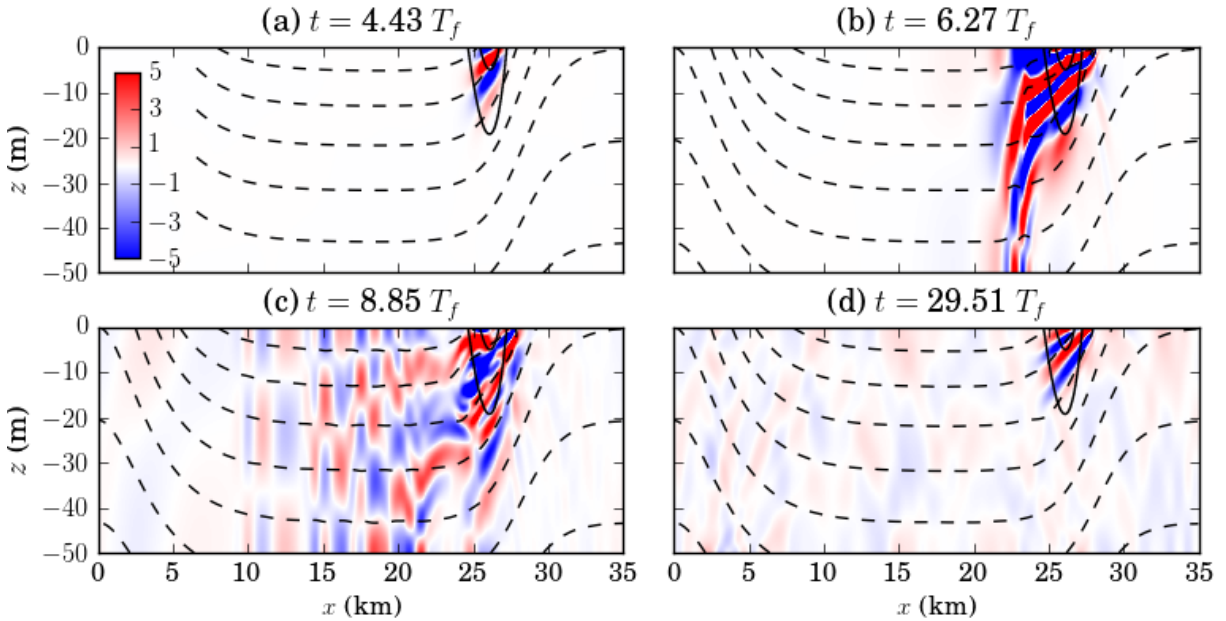

Figure 2: Snapshots of u, in mm s^{-2}. The color scale, which is common to all four panels, saturates in the unstable region, the maximum value of u in the whole time series being about 15 mm s^{-1}. Dashed contours are isopycnals, and solid contours are the initial $\sigma_0/f = 0$ and $\sigma_0/f = 0.6$ contours. $T_f = 2\pi/f \approx 61000$ s.

The second phase starts when the instability reaches the $f\overline{Q} = 0$ boundary, beyond which the flow is stable to SI, and only internal waves can propagate. So far, the growth of the SI-induced flow has been fast enough to induce perturbations, occurring over time scales of order f. Outside of the front, this frequency is also the minimum frequency at which internal waves can oscillate at. Therefore, the $f\overline{Q} = 0$ boundary is a place where internal waves, and in particular NIWs, are forced. Panel (b) of fig. 2 illustrates this second stage, where we see internal waves being radiated from the instability region.

Panel (c) of fig. 2 represents an intermediate stage in which NIWs propagate away from the front, and their generation subsides. Because our domain is horizontally periodic and vertically bounded, NIWs linger inside our domain, where they slowly decay due to viscous effects. The modal structure, visible in the middle of the domain, is of course an artifact due to the presence of a lower boundary in our domain. In the real ocean, it is likely that the structure would be more beam-like, as in panel (b).

Finally, panel (d) of fig. 2 shows a glimpse of the longer-term state of our system: NIWs are mostly gone, the SI flow is now steady, and does not generate any NIWs anymore.

The highly non-stationary nature of the process, described above, prevents any simple time series analysis of the NIW signal. Figure 3 nonetheless provides a time series of the horizontal, across-front signal near the middle of the domain, outside of the unstable front. It shows the different stages of the process: the first stage ($0 \leq t \leq 6T_f$), during which the SI grows in the front; the second stage ($6T_f \leq t \leq 10T_f$), where the front releases the initial and most powerful burst of internal waves; and for $t \geq 10T_f$, the waves keep propagating and decay. The frequency spectrum seems to contain contain $\omega \approx f$, but also $\omega \approx 2f$, and perhaps higher-frequency waves; and finally, the final stage in which NIW linger in the domain and decay due to viscosity.
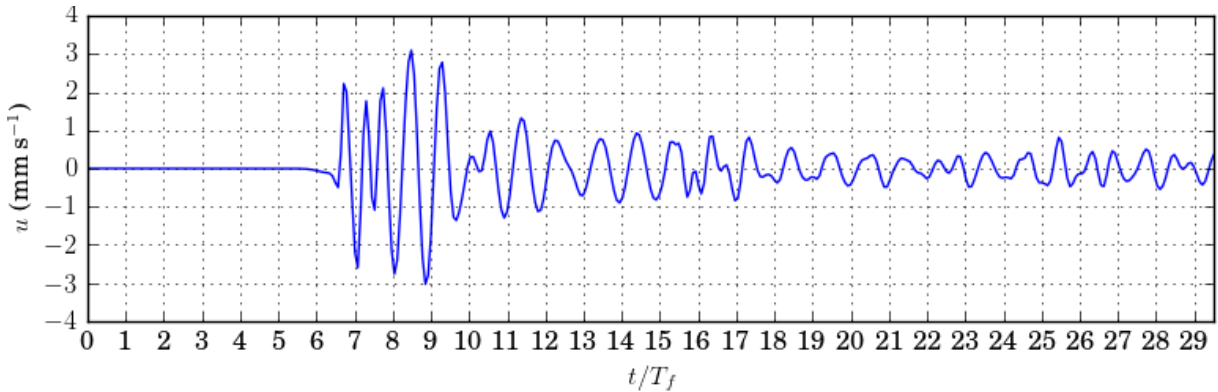

Figure 3: Time series of u at the location $(x, z) = (20$ km, -25 m). $T_f = 2\pi/f \approx 61000$ s.

5 Discussion and Conclusion

A symmetrically unstable oceanic front that is confined in two directions can be destabilized fast enough to generate NIWs. It could have significant implications for our understanding of the energy budget and life cycle of oceanic submesoscale structures. However, some of the features of our setup produced some artifacts that, while not being fatal to the relevance of this communication, are worth keeping in mind. First of all, the closed nature of our domain (horizontally periodic and bounded below) meant that NIWs linger for much longer than they would in a real ocean front. In a front, the radiated internal waves would probably look beam-like as in fig. 2(b), not mode-like like in fig. 2(c). Also, ocean fronts last for a few days before being modified by large-scale flows, instabilities, or else, and our process is not likely to happen on its own.

To our knowledge, this communication is the first to document radiation of NIWs by SI in the oceanic context. Note however that in the atmospheric context, Plougonven and Zeitlin (2009) did observe a very similar process involving inertial instability, SI's baroclinic relative. More recently, Bouchut et al. (2011) and Ribstein et al. (2014) also succinctly observe radiation of baroclinic, super-inertial NIWs radiating from symmetrically unstable geostrophic flows. Nonetheless, this process was not the focus of these articles, and more work is needed to understand it.

Our own results represent the first steps in this direction. In particular, the effects of the dimensions and strength of the front should be studied. While we chose reasonable

dimensional parameters, oceanic submesoscale fronts come in all shapes and sizes. This should be explored in order to determine which conditions, cast non-dimensionally, induce to the most significant NIW generation.

References

Alford, M. H., Shcherbina, A. Y., and Gregg, M. C. (2013). Observations of near-inertial internal gravity waves radiating from a frontal jet. *J. Phys. Oceanogr.*, 43(6):130305125949003.

Arobone, E. and Sarkar, S. (2015). Effects of three-dimensionality on instability and turbulence in a frontal zone. *J. Fluid Mech.*, 784:252–273.

Boccaletti, G., Ferrari, R., and Fox-Kemper, B. (2007). Mixed Layer Instabilities and Restratification. *J. Phys. Oceanogr.*, 37(9):2228–2250.

Bouchut, F., Ribstein, B., and Zeitlin, V. (2011). Inertial, barotropic, and baroclinic instabilities of the Bickley jet in two-layer rotating shallow water model. *Phys. Fluids*, 23(12):126601.

D'Asaro, E., Lee, C., Rainville, L., Harcourt, R., and Thomas, L. (2011). Enhanced turbulence and energy dissipation at ocean fronts. *Science*, 332(6027):318–22.

Ferrari, R. and Wunsch, C. (2009). Ocean Circulation Kinetic Energy: Reservoirs, Sources, and Sinks. *Annu. Rev. Fluid Mech.*, 41:253–282.

Gill, A. E. (1984). On the Behavior of Internal Waves in the Wakes of Storms. *J. Phys. Oceanogr.*, 14(7):1129–1151.

Grisouard, N. and Thomas, L. N. (2016). Energy Exchanges between Density Fronts and Near-Inertial Waves Reflecting off the Ocean Surface. *J. Phys. Oceanogr.*, 46(2):501–516.

Haine, T. W. N. and Marshall, J. (1998). Gravitational, Symmetric, and Baroclinic Instability of the Ocean Mixed Layer. *J. Phys. Oceanogr.*, 28(4):634–658.

Hazewinkel, J. and Winters, K. B. (2011). PSI of the Internal Tide on a β Plane: Flux Divergence and Near-Inertial Wave Propagation. *J. Phys. Oceanogr.*, 41(9):1673–1682.

Joyce, T. M., Toole, J. M., Klein, P., and Thomas, L. N. (2013). A near-inertial mode observed within a Gulf Stream warm-core ring. *J. Geophys. Res. Ocean.*, 118(4):1797–1806.

Kunze, E. and Sanford, T. B. (1984). Observations of Near-Inertial Waves in a Front. *J. Phys. Oceanogr.*, 14(3):566–581.

Loken, C., Gruner, D., Groer, L., Peltier, R., Bunn, N., Craig, M., Henriques, T., Dempsey, J., Yu, C.-H., Chen, J., Dursi, L. J., Chong, J., Northrup, S., Pinto, J., Knecht, N., and Zon, R. V. (2010). SciNet: Lessons Learned from Building a Power-efficient Top-20 System and Data Centre.

McWilliams, J. C. (2016). Submesoscale currents in the ocean. *Proc. R. Soc. A Math. Phys. Eng. Sci.*, 472(2189):20160117.

Plougonven, R. and Zeitlin, V. (2009). Nonlinear development of inertial instability in a barotropic shear. *Phys. Fluids*, 21(10):1–15.

Rainville, L. and Pinkel, R. (2004). Observations of Energetic High-Wavenumber Internal Waves in the Kuroshio. *J. Phys. Oceanogr.*, 34(7):1495–1505.

Ribstein, B., Plougonven, R., and Zeitlin, V. (2014). Inertial versus baroclinic instability of the Bickley jet in continuously stratified rotating fluid. *J. Fluid Mech.*, 743:1–31.

Shakespeare, C. J. and Taylor, J. R. (2014). The spontaneous generation of inertiagravity waves during frontogenesis forced by large strain: theory. *J. Fluid Mech.*, 757:817–853.

Stone, P. H. (1966). On Non-Geostrophic Baroclinic Stability. *J. Atmos. Sci.*, 23(4):390–400.

Taylor, J. R. and Ferrari, R. (2009). On the equilibration of a symmetrically unstable front via a secondary shear instability. *J. Fluid Mech.*, 622:103.

Thomas, L. N. (2012). On the effects of frontogenetic strain on symmetric instability and inertia–gravity waves. *J. Fluid Mech.*, 711(September):620–640.

Thomas, L. N. and Taylor, J. R. (2014). Damping of inertial motions by parametric subharmonic instability in baroclinic currents. *J. Fluid Mech.*, 743:280–294.

Thomas, L. N., Taylor, J. R., Ferrari, R., and Joyce, T. M. (2013). Symmetric instability in the Gulf Stream. *Deep Sea Res. Part II Top. Stud. Oceanogr.*, 91:96–110.

Wang, P., McWilliams, J. C., and Ménesguen, C. (2014). Ageostrophic instability in rotating, stratified interior vertical shear flows. *J. Fluid Mech.*, 755:397–428.

Whitt, D. B. and Thomas, L. N. (2013). Near-Inertial Waves in Strongly Baroclinic Currents. *J. Phys. Oceanogr.*, 43(4):706–725.

Winters, K. B. and de la Fuente, A. (2012). Modelling rotating stratified flows at laboratory-scale using spectrally-based DNS. *Ocean Model.*, 49-50(April):47–59.

Winters, K. B., MacKinnon, J. A., and Mills, B. (2004). A Spectral Model for Process Studies of Rotating, Density-Stratified Flows. *J. Atmos. Ocean. Technol.*, 21(1):69–94.